8

Motion Calculations on Stent Grafts in AAA

Almar Klein[1], W. Klaas Jan Renema[2], J. Adam van der Vliet[3],
Luuk J. Oostveen[2], Yvonne Hoogeveen[2],
Leo J. Schultze Kool[2] and Cornelis H. Slump[1]
[1]*Institute of Technical Medicine, University of Twente.*
[2]*Dept. of Radiology, Radboud University Nijmegen Medical Center.*
[3]*Dept. of Surgery, Radboud University Nijmegen Medical Center.*
The Netherlands

1. Introduction

Although endovascular aortic replacement (EVAR) has been proven to be successful (Blankensteijn et al., 2005; Zarins et al., 1999), due to the need for reintervention it does not have a significant advantage over open repair on the long term (Bruin et al., 2010; Investigators, 2010). Late stent graft failure is therefore a serious complication in endovascular repair of aortic aneurysms (Cao et al., 2009; Demirci et al., 2009; Jacobs et al., 2003; Li & Kleinstreuer, 2006; Mattes et al., 2005; Roos et al., 2005). Examples are metal fatigue, stent graft migration (Koning et al., 2006; Li & Kleinstreuer, 2006), and the formation of endoleaks (Lu et al., 2008; Stavropoulos & Charagundla, 2007).

The long-term durability of stent grafts is affected by the stresses and hemodynamic forces applied to them, which may be reflected by the movements of the stent graft itself during the cardiac cycle. Studying the dynamic behavior of stent grafts can therefore give a better understanding of their motion characteristics, and can give insights into how these motion characteristics relate to certain stent-related problems. This information will be beneficial for designing future devices and can be valuable in predicting stent graft failure in individual patients (Langs et al., 2007).

Motions of (stent grafts in) AAA can be measured using fluoroscopic roentgenographic stereophotogrammetric analysis (FRSA) (Koning et al., 2007), dynamic magnetic resonance imaging (van Herwaarden, Muhs, Vincken, van Prehn, Teutelink, Bartels, Moll & Verhagen, 2006), and ECG-gated CT (Teutelink et al., 2007). Although ultrasound is also used (van der Laan et al., 2003), it does not produce the three dimensional images that are required for the quantitative analysis of the whole stent graft. ECG-gated CT has the advantage of having high contrast for metal objects. Furthermore, ECG-gated CT is widely available, easily accessible, and can easily be applied in a post-operative setting.

To study the motions quantitatively, and to process the large datasets associated with ECG gating, automated processing is required. We divide the processing in two steps: segmentation of the stent, and calculating the motions of the stent[1].

[1] A stent graft consists of a metal frame surrounded by blood-proof material (the graft). When we only use the word "stent", we refer to the metallic frame: the graft is not visible on a CT scan.

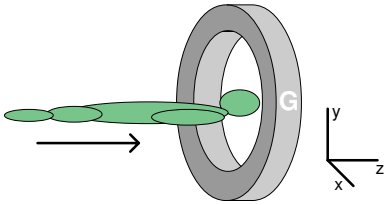

Fig. 1. Illustration of the orientation of the patient with respect to the CT scanner. The ring indicated by 'G' represents the gantry of the CT scanner.

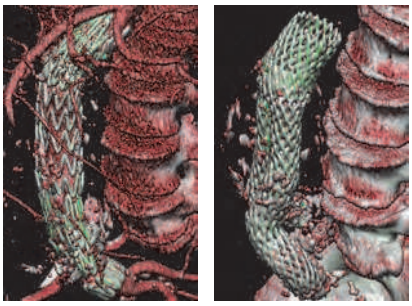

Fig. 2. Illustration of iso surfaces rendered from CT data of two types of stent grafts.

2. ECG-gated CT

In computed tomography (CT) a three-dimensional image of an object is constructed by a computer from a series of images obtained using roentgen radiation (Figure 1, Figure 2). In current CT scanners the x-ray source rotates around the object while the object is moved through the scanner in the *z*-direction. This enables scanning the complete object in one continuous (helical) motion (Kalender, 2005).

In recent years there have been major advancements in CT. Shorter rotation times and the development of multi detector CT (MDCT) enabled the technique of ECG gating, often referred to as cardiac CT (Fuchs et al., 2000). With this technique, the patient's ECG signal is measured during the scan. It is then possible to divide the raw scan data into bins that correspond to consecutive phases of the heart beat. The data in each bin is then reconstructed into a three-dimensional image (i.e. a volume), and the final result is a sequence of volumes, each corresponding to a different phase of the heart cycle (Figure 3). This allows 4D visualization of the scanned object and enables investigation to its temporal behavior (Fuchs et al., 2000; Ohnesorge et al., 2000). ECG-gated CT enables measuring motions that are synchronous with the patient's heart beat; other motions, such as those caused by breathing result in motion artifacts. The number of volumes that is reconstructed per scan is in the order of 8-20 (Hazer et al., 2009; Teutelink et al., 2007).

2.1 Dose and the noisy nature of CT data

One of the major downsides of CT in general is the exposure of the patient to ionizing radiation, which can have negative effects on the long term health of the patient (Fazel et al., 2009; Prokop, 2005). The dose should therefore be kept as low as reasonably achievable. However, this results in higher noise levels and more image artifacts, which can cause

problems for automatic image analysis algorithms that often need high quality data to operate. Algorithms that can perform their task on low dose data can therefore contribute to better patient safety.
In ECG-gated CT, multiple volumes are produced from the same amount of raw data. Assuming that the dose is kept the same, the amount of noise in each volume is therefore significantly larger than in volumes reconstructed using conventional CT.

2.2 Combining the volumes

The clinic sometimes also requires the result of a non-gated scan because of its lower levels of noise. Unfortunately, not all scanners are capable of producing a non-gated three-dimensional image in case ECG-gated scanning was used. Scanning patients twice is not an option considering the extra dose this would imply.
Averaging the data of the volumes off-line (i.e. not on the scanner's reconstruction computer) also produces a 3D dataset. This is a straightforward process, yet fundamentally different from combining the raw data (sinogram) before the filtered back-projection reconstruction (as happens for a non-gated scan). Due to non-linearities in the reconstruction process of the scanner, the results may be similar but will never be exactly the same.
In a study on phantom data acquired with a 64-slice Siemens Somatom CT scanner it was found that averaging the volumes in this way does not have negative effects on image quality in terms of noise, frequency response and motion artifacts (Klein, Oostveen, Greuter, Hoogeveen, Kool, Slump & Renema, 2009b). Rather, the noise was found to be slightly lower, and motion artifacts were found to be less severe.
For the purpose of segmentation, combining the volumes can also be advantageous. It has been shown that combining a subset of all volumes in the sequence can produce better results due to a more optimal compromise between noise and motion blur [Accepted for publication in Medical Image Analysis].

2.3 The effect of the patient's heart rate

While the patient is moved through the scanner (i.e. along the z-axis), data is collected and the patient's ECG-signal is measured (Figure 1). To construct a single volume with full coverage in the z-direction, data is collected from multiple heart beats (Figure 3). The table speed, rotation time of the scanner, and the heart beat of the patient together determine the amount of overlap in the z-direction. Negative overlap signifies a volume gap (Figure 3(b)), which is expressed as extremely noisy bands (Figure 4) that propagate through the data (the exact effects can differ per scanner). The data inside these gaps is completely unreliable (even if the scanner tries to interpolate it) because data at these positions is simply not available (Klein, Oostveen, Greuter, Hoogeveen, Kool, Slump & Renema, 2009a).
It can be shown theoretically, and it has been verified in an experiment (Klein, Oostveen, Greuter, Hoogeveen, Kool, Slump & Renema, 2009a), that there is a minimum required heart beat in order to obtain images without volume gaps. This minimum heart beat can be calculated as follows:

$$B_{min} = \frac{60 \cdot p}{T_{rot}}, \tag{1}$$

where p is the pitch factor, T_{rot} the rotation time, and B_{min} the minimum required heart rate in beats per minute. For a typical setup with $T_{rot} = 0.37$ and $p = 0.34$ the minimum required heart beat $B_{min} = 55$ bpm.

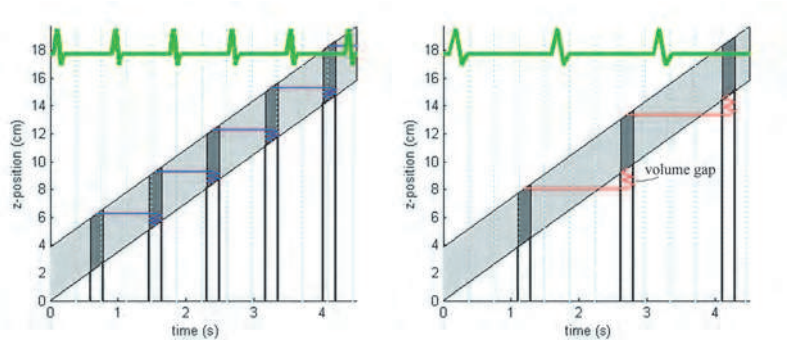

(a) 70 bpm (b) 40 bpm

Fig. 3. Diagram illustrating the process of ECG-gating. The light grey band indicates the covered z-positions of the detector during the scan. The dark grey patches represent parts of the phase in each heart beat.

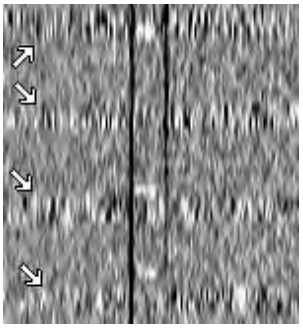

Fig. 4. Illustration of the noise bands in the CT images caused by the volume gaps due to a too low heart rate (45 bpm) during scanning. Shown is an image of a phantom which has small metal bars embedded at regular intervals. It can be seen how the second bar from the top is hidden by a noise band (i.e. volume gap).

It is noteworthy that a too high heart rate should also be avoided, since this leads to increased motion artifacts.

2.4 Temporal resolution

The temporal resolution of the technique of ECG gating consists of two parts (Figure 5): the first is the width of each phase T_w, which is fully determined by the rotation time and reconstruction algorithm. Its value determines to what extent motion causes artifacts in the resulting data. Since T_w depends on the applied reconstruction algorithm, which is often chosen by the manufacturer, this value is often unknown. In Klein, Oostveen, Greuter, Hoogeveen, Kool, Slump & Renema (2009a) a simple experiment is described to measure the value of T_w empirically.

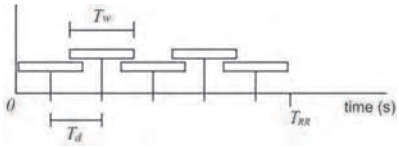

Fig. 5. Diagram illustrating the two aspects of temporal resolution. T_w is determined by the rotation time and reconstruction algorithm. T_d is determined by the heart rate and the number of reconstructed phases (five in this example).

The second part is the (temporal) distance between phases T_d, which is determined by the number of phases and the heart rate. It represents the sampling rate of the technique. If more phases are reconstructed, T_d decreases and the overlap between phases increases.
In an ideal scenario, T_w should be as low as possible to be least affected by motion artifacts, and T_d should be approximately equal such that the sampling frequency is high enough to prevent aliasing, with a minimal number of phases.

2.5 Application

ECG-gated CT is extensively used in cardiac exams (Albers et al., 2003; Manzke et al., 2004; Williamson et al., 2008), especially for the assessment of coronary arteries (Chartrand-Lefebvre et al., 2007; Dewey et al., 2008; Greuter et al., 2005). The goal in most of these studies is to limit the effect of motion rather than to examine the motion itself for which the technique can also be utilized.
Recently, ECG-gated CT was used to study the pulsating motion of AAA (Teutelink et al., 2007), and the motion of the renal arteries (Muhs, Teutelink, Prokop, Vincken, Moll & Verhagen, 2006).
The abdominal aorta is constantly in motion caused by the pressure waves from the contracting heart. However, the dynamics of this motion are more subtle than the motions present in the heart itself. It has been shown that the order of magnitude of these motions is in the order of 2 mm (Muhs, Vincken, van Prehn, Stone, Bartels, Prokop, Moll & Verhagen, 2006; Teutelink et al., 2007). It is reported that the limits of the motion that can be detected in clinical practice by ECG gating are slightly less than the spacing between the voxels (usually in the order of 0.5 mm), and that for a typical setup frequency components up to 2.7 Hz can be accurately detected (Klein, Oostveen, Greuter, Hoogeveen, Kool, Slump & Renema, 2009a). This makes ECG-gated CT a suitable technique for studying motions in AAA.

3. Segmentation of the stent graft

Segmentation of the stent graft is performed on a three-dimensional image. Depending on how the data is processed further, the segmentation is applied to all volumes in the sequence, or to a single volume obtained by combining the volumes in the sequence.
Several studies have been published on the segmentation of blood vessels in 3D, which have correspondences with the wires of the frame of the stent and may therefore be of interest (see Lesage et al. (2009) and Kirbas & Quek (2004) for an overview of vessel segmentation methods). Methods that fit a series of spheres or ellipsoids to the vessel (Beck et al., 2009; Zhou et al., 2008), and methods that segment the contour in slices perpendicular to the vessel centerline (Hernandez-Hoyos et al., 2002; Lee et al., 2007) assume a solid vessel with a diameter of several voxels. Due to the small diameter of stent wires (1 to 3 voxels) and their

sharp corners, these methods are not suitable for the segmentation of stents. Region growing methods (Bock et al., 2008) have problems with leaks and gaps and need a second stage to find the geometry from the segmented voxels. A common method is the two-step approach (Freiman et al., 2009; Kaftan et al., 2009; Manduca et al., 2009; Worz et al., 2009), which first segments the vessel using a vessel measure (Frangi et al., 1998) followed by centerline tracking. This method, however, is known to have difficulties where the structure is not tubular, such as in crossings and sharp corners in the stent's frame.
A related method is used by Langs et al. (2011) for the segmentation of stent grafts in the aortic arch. Interest points are extracted that are located on the center line of the stent determined by a skeletonization of the volume thresholded at 2000 Hounsfield units (HU) and weighted by its vesselness measure (Frangi et al., 1998). The result is a dense set of points that lie on the frame of the stent.
Unfortunately, the *quality of the data*—defined as how well the frame of the stent is distinguishable in the data—is not always sufficient for such a method to fully segment the stent's frame (Klein et al., 2008). This quality depends on the combination of used dose, stent wire diameter, material properties of the stent (i.e. absorption coefficient), and patient anatomy. The stent can consist of CT values as low as 300 HU (Klein et al., 2008). There are also reports of some stent types being barely distinguishable, whereas other stent types are well visible in data obtained using the same scanner settings [Submitted to Medical Image Analysis].
In addition to the bad visibility of the frame of the stent, several problems can be identified for (low dose) CT data. Firstly, the data is relatively noisy. Secondly, streak artifacts occur where the stent's metal frame is thick or where a coil is present next to the stent graft. Thirdly, contrast agent injected in the blood results in CT-values close to the range of CT-values seen for most stents. Fourthly, due to image artifacts, the wire of the stent sometimes contains gaps. In this section, we discuss a way to model the stent graft, and two approaches to obtain such a model from the volumetric CT data in ways that are relatively robust for the aforementioned problems.

3.1 Modeling the stent

Most studies related to the motion of stent grafts focus on measuring the stent's diameter changes (van Herwaarden, Bartels, Muhs, Vincken, Lindeboom, Teutelink, Moll & Verhagen, 2006) or determining the motion at a sparse set of points on the stent (Langs et al., 2007). A model that enables capturing material properties and high level knowledge regarding the stent graft characteristics would be valuable to gain more insight in the stent's in vivo behavior (Langs et al., 2007). Furthermore, such a model can also help in performing more reliable (fluid dynamics) simulations, which is important for improving current stent designs (Cebral et al., 2009; Kleinstreuer et al., 2007).
In [submitted to Medical Image Analysis] a geometric model is proposed that represents the wire frame of the stent as an undirected graph, with nodes placed at the corners and crossings of the frame, and the edges between the nodes representing the wires (Figure 6). This model can be applied to different stent types, and represents the topology of the stent's frame in a concise and natural way.

3.2 Segmentation of the stent graft via centerline tracking

A stent has a tubular structure, sometimes with branches, and can be approximated by a series of stacked contours which are orthogonal to the centerline (Figure 7). An approach

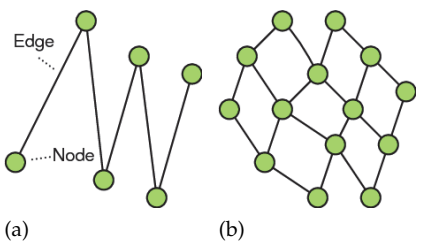

Fig. 6. Example graphs that describe a geometric model of a stent frame. The edges between the nodes represent the physical wire frame of the stent. Nodes are placed at corners (a) and crossings (b).

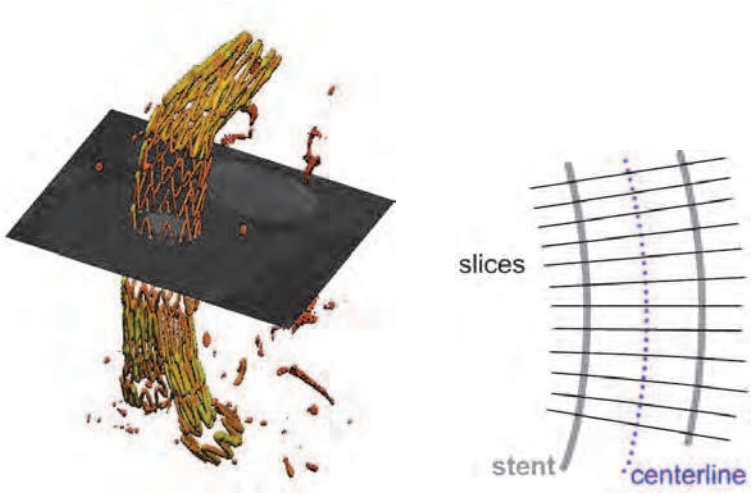

Fig. 7. Illustration of how the stent can be approximated as a series of stacked contours. (a) shows a volume rendering of the stent and a slice orthogonal to its centerline. (b) shows a schematic illustration of contours perpendicular to the stent's centerline.

published by Klein et al. (2008) is to segment the stent in 2D images sampled perpendicular to its centerline. Regions with high CT-values (typically above 500 HU) exist where the metallic frame of the stent penetrates the image. These regions have high CT-values and—due to their "pointy" structure—well suited for point detection.

The approach to segment the stent in these 2D images is to first detect a set of interest points, after which a clustering algorithm is applied to find the points that are on the wire of the stent. This process is then repeated in an iterative fashion, while tracking along the centerline of the stent. At the end of this process, a 3D geometric model of the stent is obtained.

An advantage of this approach is that part of the algorithm is 2D, which makes visualization and algorithm design easier. A disadvantage is that modeling the stent as a series of stacked contours causes difficulties at bifurcations and when parts of the frame of the stent overlap.

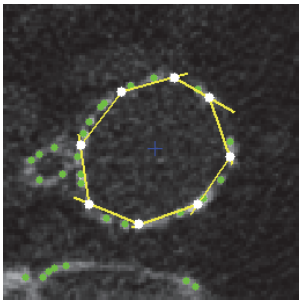

Fig. 8. Example of the clustering algorithm after finding a coarse contour.

3.2.1 Point detection

Four different point detection algorithms were taken into consideration and tested in an experiment. An algorithm based on the product of Eigenvalues was found to work the best. This measure, also known as the Gaussian curvature, can be expressed using image derivatives: $\frac{\partial^2 L}{\partial x^2} \cdot \frac{\partial^2 L}{\partial y^2}$, where L is the 2D image. Other methods taken into consideration were a static threshold, a dynamic threshold, and the Laplacian (the sum of Eigenvalues).

3.2.2 Clustering

Four different clustering algorithms were taken into consideration and tested in an experiment. The best method was found to be a custom method that uses a virtual stick to select the stent-points in an iterative fashion. By selecting points from the inside of the contour, spurious points outside of the contour are ignored (Figure 8). Other clustering methods taken into consideration were circle fitting, ellipse fitting, and GVF snakes (Xu & Prince, 1998).
The result of the clustering method is a set of points that represent the contour of the stent. By fitting a circle on these points, an estimate of the radius and center position can be obtained, which are used during centerline tracking.

3.2.3 Centerline tracking and modeling

Starting from a manually selected seed point, the algorithm tracks the stent in both directions. Starting from a coarse estimate of the centerline orientation, slices are sampled, to which the aforementioned algorithms are applied. The center position found at each slice is used to estimate the next centerline position. For the method to be less sensitive to noise present on the center estimate (caused by the discrete nature of the contour points), a smoothness constraint is adopted. Bifurcations are detected when a significant change in the diameter estimate is encountered. Subsequently, both branches of the bifurcations are tracked individually.
To deal with the gaps between the different parts of the stent graft that are present in some stent types (Figure 7(a)), the tracking will proceed in the last known direction if no contour could be found. When no contour is found along a predefined distance, it is assumed that the end of the stent is reached, and the tracking stops.
During centerline tracking the contour points in the current slice are matched to the contour points of the previous slice. In this fashion the individual wires are tracked too. The positions where two wires meet—which represent the corners and crossings of the stent's frame—are detected, and nodes are created at these positions to build the geometric model (Figure 9).

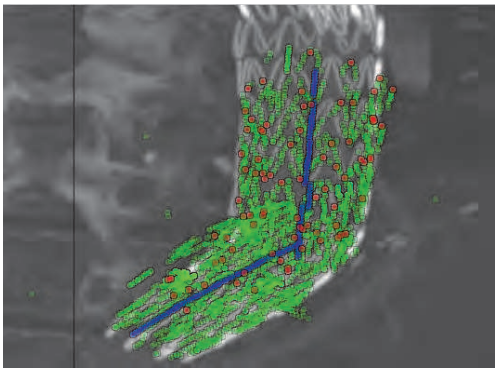

Fig. 9. Illustration of the centerline tracking algorithm in progress. The blue dots indicates the found centerline. The green dots indicate the found stent points, and the larger red dots indicate the found nodes which will be connected to form a geometrical model.

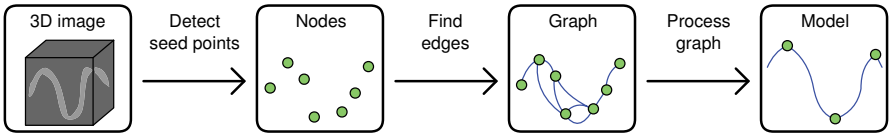

Fig. 10. Flowchart illustrating the three processing steps of the MCP-based algorithm to extract a geometrical model from the CT data.

3.3 Segmentation of the stent graft via the minimum cost path method

A method to segment the stent graft in 3D by finding the optimal paths between a large set of automatically detected seed points is proposed in [submitted to Medical Image Analysis]. The method can be divided into three steps, which are illustrated in the flow chart in Figure 10.

3.3.1 Detection of seed points

In the first step, a set of seed points is found by searching the volume for voxels subject to three criteria: 1) The voxel intensity must be a local maximum. 2) The voxel intensity must be higher than a predefined threshold value. 3) The voxel must have a direct neighbor with an intensity also above this threshold value.

3.3.2 Finding the optimal paths

In the second step, the seed points are connected using a modified version of the minimum cost path (MCP) method. The MCP method can be used for segmentation of vessels and other structures (e.g. (Cohen & Deschamps, 2007; Deschamps & Cohen, 2000; Fahmi et al., 2008; Gülsün & Tek, 2008; Jandt et al., 2009; Quek & Kirbas, 2001; Wink et al., 2004)). It is a level set method in which a front is propagated monotonically following a (non-negative) cost function. The advantages of this method are that it can be implemented in a computationally efficient way, and that it can easily be modified to make it more suitable for a specific problem, see for example Klein, Renema, Kool & Slump (2009) and Cohen & Deschamps (2007).
To use the MCP method for stent segmentation, it is modified such that the fronts evolve from all the seed points found in the seed point detection step. Connections between the nodes

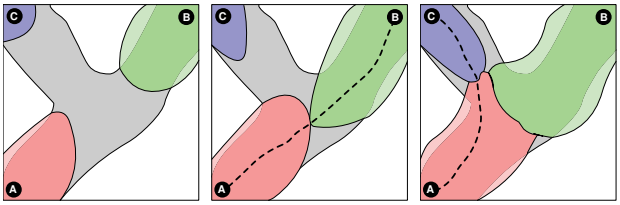

(a) (b) (c)

Fig. 11. Illustration of three meeting fronts in the MCP algorithm. The black circular shapes indicate seed points A, B and C. In (a) the fronts do not yet meet. In (b) front A meets front B, and the path is traced. A few iterations later, in (c) a third front meets with the first, connection seed points A and C.

are detected when two fronts collide, and the paths between the points are found using a backtrace map that is maintained during the evolution of the front.
The result of the MCP algorithm is a graph consisting of nodes (the seed points) connected by edges. Each edge is associated with a path of voxels connecting one node to another. However, many of these edges are false edges and have to be removed.

3.3.3 Graph processing

In the third step, the false edges are removed using graph processing techniques. For this purpose, two scalar values are associated with each edge. The first is α, the maximum cumulative cost on the path. It represents the *weakness* (i.e. inverse strength) of the edge. This value is used to establish the order of the edges; a stronger connection (lower α) is preferred over a weaker one. The second scalar value is β, the minimum intensity (the CT-value in Hounsfield Units) on the path. Due to the definition of CT-values (-1000 representing air and 0 representing water) this value has a physical meaning and represents the *quality* of the edge; it is used to determine whether an edge should be removed or not.
The processing of the graph occurs in multiple different passes. Firstly, weak edges are removed based on the expected number of edges for each node. This value depends on the specific stent type being segmented. The weakness value α is used to establish the weakest edges to consider for removal, and the quality measure β is used to determine whether an edge should be removed. Secondly, a clean-up pass is performed to remove redundant edges; an edge is found redundant if there is a path of one or two stronger (i.e. lower α) edges that connect the same nodes. Thirdly, corners are detected in the wire, and nodes are placed at the positions that have the highest curvature. Hereafter the graph is cleaned up again. Fourthly, crossings are detected and nodes are added to represent them. Finally, after a final clean-up step, all the paths are smoothed.

3.3.4 Experiments and results

To evaluate the quality of the geometric model produced by this method, experiments were performed in which the model was compared with a reference model annotated by three experts. By counting the number of corresponding edges, a similarity measure was obtained. A training set was used to obtain the optimal parameter values of the algorithm, and using a test set the final performance of the method was evaluated.

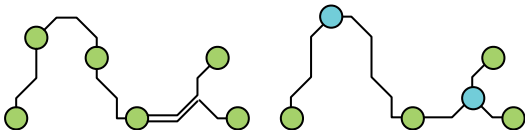

(a) Before (b) After

Fig. 12. Illustration of adding corners and nodes. In (b) two nodes were removed and a node was placed at the corner. Another node was inserted at the crossing.

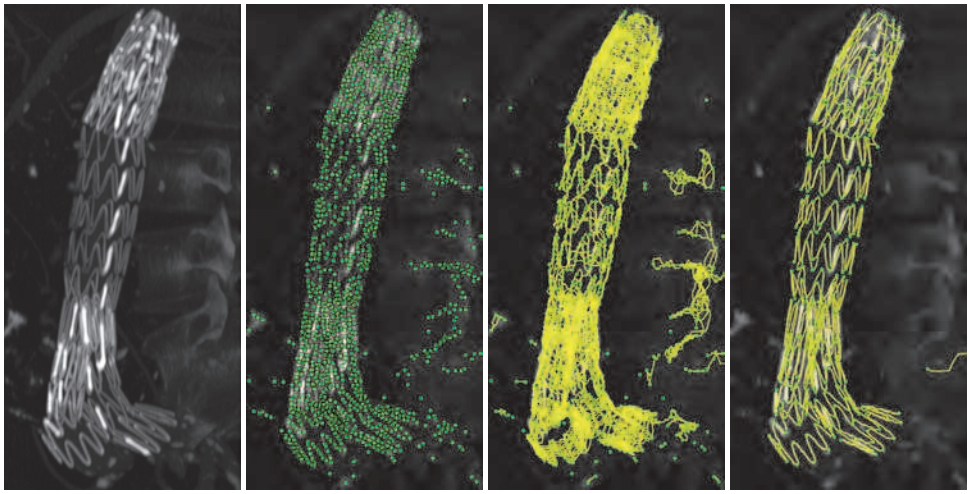

(a) MIP of the CT data (b) 1732 seed points (c) 4963 initial edges (d) 531 final edges

Fig. 13. Illustration of the different algorithm steps. Shown are a Maximum Intensity Projection (MIP) of the original data (a), the detected seed points (b), the found edges (c), the result after processing the graph (d).

The algorithm was found to be robust for variations in its parameter values, and for the high noise levels present in the data. The found similarity with the reference data was found to be 96% and 92% for the two stent types considered in the experiments. Visual inspections of the results showed that most errors were present in difficult areas of the stent, such as bifurcations and narrow legs where the wire has relatively sharp corners.
An example of the results after each processing step is shown in Figure 13. In Figure 14 lit surface renders are shown for the found geometric models of three datasets.

4. Calculating motions and forces of the stent graft

When the geometric model of the stent is obtained, it can be used as a tool to study the motions of the stent graft. For this purpose, motion is applied to the model. In the first part of this section we discuss how this can be done, following the ideas presented in [Accepted for publication in Medical Image Analysis]. In the second part of this section we discuss an alternative method that uses active shape models to study stent graft motions.

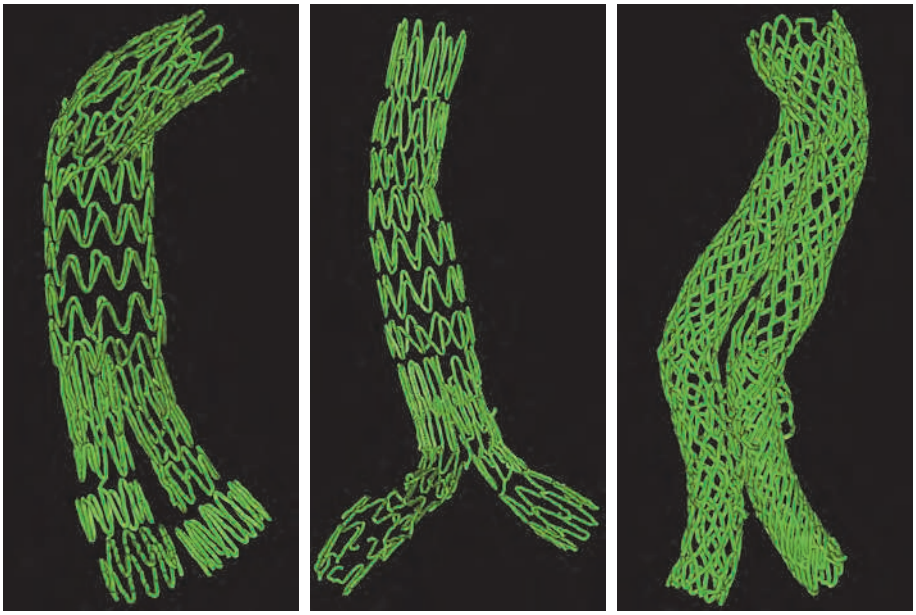

Fig. 14. Illustration of lit surface renders of the geometric models for three example stent grafts.

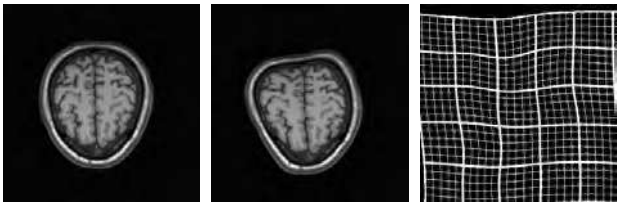

(a) Image A (b) Image B (c) Deformation field

Fig. 15. An example of registering two images, and the resulting deformation field.

4.1 Motion analysis using a geometric model

The motion of interest is obtained from the sequence of CT volumes using a registration algorithm. The purpose of a registration algorithm is to (elastically) align two images; the result is a deformation field that describes how one image should be deformed to align it with the second (Figure 15). This deformation field can be applied to the geometric model to enable studying the motions.

4.1.1 Image registration

The current range of common region based image registration algorithms can be divided into two classes. Both classes usually adopt a multiscale approach in order to prevent finding a local minimum, and to speed up the registration process. The first class employs a B-spline grid to describe the deformation field, which is optimized by minimizing/maximizing a

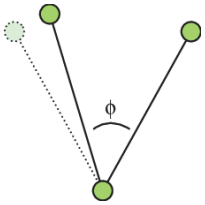

Fig. 16. Illustration of how the (change of) angle ϕ can be used to a estimate the force present in the node when motion is applied to the model.

similarity measure. Using Mutual Information (MI) as a similarity measure, these methods have been shown to be robust for differences in the appearance between the images (Maintz & Viergever, 1998; Rueckert et al., 1999; Wells et al., 1996). While the use of a B-spline grid can cause problems when describing rotational deformations (Kroon & Slump, 2009), it has the advantage that the deformations are described in an efficient way and are physically realistic (Noblet et al., 2006). Additionally, the deformations can be regularized in various ways, for example by minimizing bending energies or penalizing small Jacobians (Rueckert et al., 1999). The second class uses image forces calculated at the pixels/voxels to drive the registration process. A popular example is the Demons algorithm (Thirion, 1998), which is related to optical flow. The deformation is obtained for each pixel individually by calculating image forces, and regularization of the deformation field is performed by Gaussian diffusion. The Demons algorithm is capable of handling extreme deformations, which can also be a downside, since such deformations are usually not physically realistic. Another problem with the Demons algorithm is that it assumes pixel intensities in corresponding regions between images to be similar, which causes problems in images containing much noise or artifacts such as bias fields (Noblet et al., 2006).
It is of importance to select the right registration algorithm for each problem, and to choose the best parameters, of which most registration algorithms have many (Klein et al., 2010). In the case of registering the different volumes obtained by ECG-gated CT, the used registration algorithm should be accurate in order to deal with the small motions present in AAA, and should be robust for noise and other artifacts associated with low dose CT. Which algorithms qualify for this task is currently being investigated.

4.1.2 Analysis of motion and forces

The result of the registration algorithm is a deformation field that describes the deformation for each voxel in the volume. To study the motions of a stent, the deformation field is applied to the nodes of the geometric model: for each node the deformation is applied that corresponds to its location in the volume. This will allow quantitative studies to the motion patterns of individual stents, and allows comparison between patients.
Because the topology of the stent is fully captured by the geometric model, the forces acting on the stent's frame can be estimated by incorporating material properties such as stiffness, and by calculating the change of the angle between two edges (Figure 16).

4.2 Motion analysis using active shape models

A technique of interest for the evaluation of motions of stent grafts is that of Langs et al. (2011). Their application is for stent grafts in the aortic arch to treat aortic ruptures caused by trauma. In Langs et al. (2007) a method for the unsupervised learning of models from sets of

interest points was proposed. It is based on minimum description length (MDL) group-wise registration (Thodberg, 2003). The global and local deformation are captured using a statistical deformation model that is built during registration of a sparse set of interest points. No a priori annotation, or definition of topological properties of the structure is necessary.
Instead of deforming the whole volume they search for correspondences between finite lists of interest points and local features in the data. This has a few advantages: 1) The algorithm can omit variations that are not relevant to the model. 2) The approach is not constrained to an a priori topological class because it does not rely on a mapping to a reference image. 3) No prior segmentation of the object is necessary, only the interest point extraction method has to be chosen according to the structure of interest. A disadvantage of this approach, however, is that it is less accurate than texture-based registration with which registration errors smaller than the voxel size can be obtained (Klein et al., 2011; Murphy et al., 2011). This can be a problem for stent grafts in AAA, because—due to the larger distance from the heart—the motions are smaller than in the aortic arch.

4.2.1 MDL registration

First a set of interest points is detected in each volume of the ECG-gate sequence. These points are treated as landmarks candidates; each landmark is associated with a position (x, y, z) and local features (such as image intensity and steerable filters). The registration is initialized by pairwise matching of a subset of the interest points. Starting from these correspondences group-wise registration is performed by minimizing a criterion function that captures the compactness of the model comprising the variation of landmark positions and local feature variation at the landmark positions. The minimum description length criterion accounts for the fact that the landmarks located on the stent move in a highly correlated manner during the cardiac cycle.
The registration is optimized by a combination of k-D trees and genetic-optimization, and is followed by a refinement using a direct search. The optimization process results in a shape variation model, which is then used to study the motions of the stent.

4.2.2 Motion analysis

The analysis of the stent deformation during the cardiac cycle is performed using the shape model that results from the group wise registration (Figure 17). For each landmark the positions in all volumes in the sequence are known. Three measurements can be obtained for each landmark: 1) The modes of variation of the statistical shape model, which capture the correlation between landmark movements. 2) The displacement of the landmarks, which reflect the absolute movement in the anatomical environment. 3) The compactness of the local shape model build with the closest landmarks, which gives an indication about the complexity of the local deformation. This last measure is particularly of interest, since it is well suited to show regions of potential stress to the material.

5. Outlook

An automated method to quantitatively study the motions and forces of stent grafts in vivo enables studying the motion patterns of individual patients, relate them to data of a previous date, or relate them to the motion patterns of other patients.
It would also be interesting to study the range of motion patterns of stent grafts in patients without problems, and compare them to the motions in patients who do have problems. Such

Fig. 17. Global deformation (color-coded) for a few stent grafts. (Image courtesy of G. Langs from Langs et al. (2011).)

studies would, however, require large datasets to incorporate all the variabilities in motion patterns, particularly because problems with stent grafts are relatively rare. Nevertheless, we believe that such studies can help our understanding of the dynamics and failure of stent grafts, and can thereby help in designing better stent grafts in the future. Further, we hope that we are able to correlate certain distinct motion patterns to specific stent-related problems, so that this technique can be used for diagnostic purposes and prediction of stent failure.

6. Conclusion

Using ECG-gated CTA, information about the motion of stent grafts in AAA can be obtained. Using segmentation methods, a geometric model of the stent can be obtained that describes the topology of the stent in a compact way. Using registration techniques, the deformation field can be found, which can then be applied to the found geometric model. Thereby the motions of the stent graft are known in great detail, and enables calculating the forces acting on the stent. Both parameters (motion and force) provide new information that can be used in further analysis of in vivo stent graft behavior and future device design.

7. References

Albers, J., Boese, J. M., Vahl, C. F. & Hagl, S. (2003). In vivo validation of cardiac spiral computed tomography using retrospective gating, *The Annals of Thoracic Surgery* 75: 885—889.

Beck, T., Biermann, C., Fritz, D., Dillmann, R., Pluim, J. P. W. & Dawant, B. M. (2009). Robust model-based centerline extraction of vessels in CTA data, *Proc. of SPIE*, Vol. 7259, Lake Buena Vista, FL, USA, p. 72593O.

Blankensteijn, J. D., de Jong, S. E., Prinssen, M., van der Ham, A. C., Buth, J., van Sterkenburg, S. M., Verhagen, H. J., Buskens, E., Grobbee, D. E. & the Dutch Randomized Endovascular Aneurysm Management (DREAM) Trial Group (2005). Two-Year outcomes after conventional or endovascular repair of abdominal aortic aneurysms, *N Engl J Med* 352(23): 2398–2405.

Bock, S., Kuhhnel, C., Boskamp, T. & Peitgen, H. (2008). Robust vessel segmentation, *Proc. of SPIE*, Vol. 6915, San Diego, CA, USA, p. 691539.

Bruin, J. L. D., Baas, A. F., Buth, J., Prinssen, M., Verhoeven, E. L., Cuypers, P. W., van Sambeek, M. R., Balm, R., Grobbee, D. E., Blankensteijn, J. D. & the DREAM Study Group

(2010). Long-Term outcome of open or endovascular repair of abdominal aortic aneurysm, *N. Engl. J. Med.* 362(20): 1881–1889.

Cao, P., Rango, P. D., Parlani, G. & Verzini, F. (2009). Durability of abdominal aortic endograft with the talent unidoc stent graft in common practice: Core lab reanalysis from the TAURIS multicenter study, *J. Cardiovasc. Surg.* 49(4): 859–865.

Cebral, J., Mut, F., Appanaboyina, S., Lohner, R., Miranda, C., Escrivano, E., Lylyk, P., Putman, C., Hu, X. P. & Clough, A. V. (2009). Image-based analysis of blood flow modification in stented aneurysms, *Proc. of SPIE*, Vol. 7262, Lake Buena Vista, FL, USA, p. 72621G.

Chartrand-Lefebvre, C., Cadrin-Chenevert, A., Bordeleau, E., Ugolini, P., Ouellet, R., Sablayrolles, J. & Prenovault, J. (2007). Coronary computed tomography angiography: Overview of technical aspects, current concepts, and perspectives, *Canadian Association of Radiology* 58: 92—108.

Cohen, L. D. & Deschamps, T. (2007). Segmentation of 3D tubular objects with adaptive front propagation and minimal tree extraction for 3D medical imaging, *Comput Methods Biomech Biomed Engin* 10(4): 289.

Demirci, S., Manstad-Hulaas, F., Navab, N., Miga, M. I. & Wong, K. H. (2009). Quantification of abdominal aortic deformation after EVAR, *Proc. of SPIE*, Vol. 7261, Lake Buena Vista, FL, USA, p. 72611U.

Deschamps, T. & Cohen, L. D. (2000). Fast extraction of minimal paths in 3D images and applications to virtual endoscopy, *Med Image Anal* 5: 281—299.

Dewey, M., Teige, F., Rutsch, W., Schink, T. & Hamm, B. (2008). CT coronary angiography: Influence of different cardiac reconstruction intervals on image quality and diagnostic accuracy, *European Journal of Radiology* 67: 92—99.

Fahmi, R., Jerebko, A., Wolf, M. & Farag, A. A. (2008). Robust segmentation of tubular structures in medical images, *Proc. of SPIE*, San Diego, CA, USA, p. 691443.

Fazel, R., Krumholz, H. M., Wang, Y., Ross, J. S., Chen, J., Ting, H. H., Shah, N. D., Nasir, K., Einstein, A. J. & Nallamothu, B. K. (2009). Exposure to Low-Dose ionizing radiation from medical imaging procedures, *New England Journal of Medicine* 361(9): 849–857.

Frangi, A. F., Niessen, W. J., Vincken, K. L. & Viergever, M. A. (1998). Multiscale vessel enhancement filtering, *Lect Notes Comput Sci* 1496: 130—137.

Freiman, M., Joskowicz, L., Sosna, J., Miga, M. I. & Wong, K. H. (2009). A variational method for vessels segmentation: algorithm and application to liver vessels visualization, *Proc. of SPIE*, Vol. 7261, SPIE, Lake Buena Vista, FL, USA, p. 72610H.

Fuchs, T. O., Kachelriess, M. & Kalender, W. A. (2000). System performance of multislice spiral computed tomography, *IEEE Eng Med Biol Mag* 19: 63—70.

Greuter, M. J. W., Dorgelo, J., Tukker, W. G. J. & Oudkerk, M. (2005). Study on motion artifacts in coronary arteries with an anthropomorphic moving heart phantom on an ECG-gated multidetector computed tomography unit, *European Radiology* 5: 995—1007.

Gülsün, M. A. & Tek, H. (2008). Robust vessel tree modeling, *Med Image Comput Comput Assist Interv* 11: 602–611.

Hazer, D., Finol, E. A., Kostrzewa, M., Kopaigorenko, M., Richter, G., Dillmann, R., Hu, X. P. & Clough, A. V. (2009). Computational biomechanics and experimental validation of vessel deformation based on 4D-CT imaging of the porcine aorta, *Proc. of SPIE*, Vol. 7262, Lake Buena Vista, FL, USA, p. 72621F.

Hernandez-Hoyos, M., Orkisz, M., Puech, P., Mansard-Desbleds, C., Douek, P. & Magnin, I. E. (2002). Computer-assisted analysis of three-dimensional MR angiograms, *Radiographics* 22(2): 421—436.

Investigators, T. U. K. E. T. (2010). Endovascular versus open repair of abdominal aortic aneurysm, *N. Engl. J. Med.* 362(20): 1863–1871.

Jacobs, T. S., Won, J., Gravereaux, E. C., Faries, P. L., Morrissey, N., Teodorescu, V. J., Hollier, L. H. & Marin, M. L. (2003). Mechanical failure of prosthetic human implants: A 10-year experience with aortic stent graft devices, *J. Vasc. Surg.* 37(1): 16–26.

Jandt, U., Schäfer, D., Grass, M. & Rasche, V. (2009). Automatic generation of 3D coronary artery centerlines using rotational x-ray angiography, *Med Image Anal* 13(6): 846–858.

Kaftan, J. N., Tek, H., Aach, T., Pluim, J. P. W. & Dawant, B. M. (2009). A two-stage approach for fully automatic segmentation of venous vascular structures in liver CT images, *Proc. of SPIE*, Vol. 7259, Lake Buena Vista, FL, USA, p. 725911.

Kalender, W. A. (2005). *Computed Tomography*, Publicis Corporate Publishing, Erlangen.

Kirbas, C. & Quek, F. (2004). A review of vessel extraction techniques and algorithms, *ACM Comput. Surv.* 36(2): 81–121.

Klein, A., Kroon, D., Hoogeveen, Y., Kool, L. J. S., Renema, W. K. & Slump, C. H. (2011). Multimodal image registration by edge attraction and regularization using a b-spline grid, *Proc. of SPIE*, Orlando, USA, pp. 7962–71.

Klein, A., Oostveen, L. J., Greuter, M. J. W., Hoogeveen, Y., Kool, L. J. S., Slump, C. H. & Renema, W. K. J. (2009a). Detectability of motions in AAA with ECG-gated CTA: a quantitative study, *Medical Physics* 36(10): 4616–4624.

Klein, A., Oostveen, L. J., Greuter, M. J. W., Hoogeveen, Y., Kool, L. J. S., Slump, C. H. & Renema, W. K. J. (2009b). Diagnostic quality of time-averaged ECG-gated CT data, *Proceedings of SPIE*, Lake Buena Vista, FL, USA, pp. 725836–725836–6.

Klein, A., Renema, W. K., Kool, L. J. S. & Slump, C. H. (2009). Initial steps towards automatic segmentation of the wire frame of stent grafts in CT data, *Proc. of IEEE-EMBS Benelux Chapter*, Enschede, The Netherlands, pp. 116—119.

Klein, A., Renema, W. K., Oostveen, L. J., Kool, L. J. S. & Slump, C. H. (2008). A segmentation method for stentgrafts in the abdominal aorta from ECG-gated CTA data, *Proc. of SPIE*, San Diego, CA, USA, p. 69160R.

Klein, S., Staring, M., Murphy, K., Viergever, M. & Pluim, J. (2010). elastix: A toolbox for Intensity-Based medical image registration, *Medical Imaging, IEEE Transactions on* 29(1): 196–205.

Kleinstreuer, C., Li, Z. & Farber, M. A. (2007). Fluid-Structure interaction analyses of stented abdominal aortic aneurysms, *Annu Rev Biomed Eng* 9: 169—204.

Koning, O. H. J., Kaptein, B. L., Garling, E. H., Hinnen, J. W., Hamming, J. F., Valstar, E. R. & van Bockel, J. H. (2007). Assessment of three-dimensional stent-graft dynamics by using fluoroscopic roentgenographic stereophotogrammetric analysis, *Journal of Vascular Surgery: Official Publication, the Society for Vascular Surgery [and] International Society for Cardiovascular Surgery, North American Chapter* 46(4): 773–779.

Koning, O. H., Oudegeest, O. R., Valstar, E. R., Garling, E. H., van der Linden, E., Hinnen, J. W., Hamming, J. F., Vossepoel, A. M. & van Bockel, J. H. (2006). Roentgen stereophotogrammetric analysis: An accurate tool to assess Stent-Graft migration, *Journal of Endovascular Therapy* 13(4): 468—475.

Kroon, D. & Slump, C. H. (2009). MRI modalitiy transformation in demon registration, *Proceedings of the Sixth IEEE international conference on Symposium on Biomedical Imaging: From Nano to Macro*, IEEE Press, Boston, Massachusetts, USA, pp. 963–966.

Langs, G., Paragios, N., Desgranges, P., Rahmouni, A. & Kobeiter, H. (2011). Learning deformation and structure simultaneously: In situ endograft deformation analysis, *Medical Image Analysis* 15(1): 12–21.

Langs, G., Paragios, N., Donner, R., Desgranges, P., Rahmouni, A. & Kobeiter, H. (2007). Motion analysis of endovascular Stent-Grafts by MDL based registration, *Proc IEEE Int Conf Comput Vis*, pp. 1–8.

Lee, J., Beighley, P., Ritman, E. & Smith, N. (2007). Automatic segmentation of 3D micro-CT coronary vascular images, *Med Image Anal* 11: 630—647.

Lesage, D., Angelini, E. D., Bloch, I. & Funka-Lea, G. (2009). A review of 3D vessel lumen segmentation techniques: Models, features and extraction schemes, *Med Image Anal* 13(6): 819–845.

Li, Z. & Kleinstreuer, C. (2006). Analysis of biomechanical factors affecting stent-graft migration in an abdominal aortic aneurysm model, *J Biomech* 39: 2264—2273.

Lu, J., Egger, J., Wimmer, A., Grosskopf, S., Freisleben, B., Miga, M. I. & Cleary, K. R. (2008). Detection and visualization of endoleaks in CT data for monitoring of thoracic and abdominal aortic aneurysm stents, *Proc. of SPIE*, Vol. 6918, SPIE, San Diego, CA, USA, p. 69181F.

Maintz, A. J. B. & Viergever, M. A. (1998). A survey of medical image registration, *Medical Image Analysis* 2(1): 1—37.

Manduca, A., Fletcher, J. G., Wentz, R. J., Shields, R. C., Vrtiska, T. J., Siddiki, H., Nielson, T., Hu, X. P. & Clough, A. V. (2009). Reproducibility of aortic pulsatility measurements from ECG-gated abdominal CTA in patients with abdominal aortic aneurysms, *Proc. of SPIE*, Vol. 7262, SPIE, Lake Buena Vista, FL, USA, p. 72620L.

Manzke, R., Kohler, T., Nielsen, T., Hawkes, D. & Grass, M. (2004). Automatic phase determination for retrospectively gated cardiac CT, *Medical Physics* 31: 3345—3362.

Mattes, J., Steingruber, I., Netzer, M., Fritscher, K., Kopf, H., Jaschke, W. & Schubert, R. (2005). Spatio-temporal changes and migration of stent grafts after endovascular aortic aneurysm repair, *Int. Congr. Ser.* 1281: 393–397.

Muhs, B. E., Teutelink, A., Prokop, M., Vincken, K. L., Moll, F. L. & Verhagen, H. J. M. (2006). Endovascular aneurysm repair alters renal artery movement: a preliminary evaluation using dynamic CTA, *Journal of Endovacular Therapy* 13(4): 476—480.

Muhs, B. E., Vincken, K. L., van Prehn, J., Stone, M. K., Bartels, L. W., Prokop, M., Moll, F. L. & Verhagen, H. J. (2006). Dynamic Cine-CT angiography for the evaluation of the thoracic aorta; insight in dynamic changes with implications for thoracic endograft treatment, *Eur J Vasc Endovasc Surg* 32(5): 532—536.

Murphy, K., van Ginneken, B., Klein, S., Staring, M., de Hoop, B., Viergever, M. & Pluim, J. (2011). Semi-automatic construction of reference standards for evaluation of image registration, *Medical Image Analysis* 15(1): 71–84.

Noblet, V., Heinrich, C., Heitz, F. & Armspach, J. (2006). Retrospective evaluation of a topology preserving non-rigid registration method, *Medical Image Analysis* 10(3): 366–384.

Ohnesorge, B., Flohr, T., Becker, C., Kopp, A. F., Schoepf, U. J., Baum, U., Knez, A., Klingenbeck-Regn, K. & Reiser, M. F. (2000). Cardiac imaging by means of electrocardiographically gated multisection spiral CT: initial experience, *Radiology* 217: 564—571.

Prokop, M. (2005). New challenges in MDCT, *European Journal of Radiology* 15: 35—45.

Quek, F. & Kirbas, C. (2001). Vessel extraction in medical images by wave-propagation and traceback, *IEEE Trans Med Imaging* 20(2): 117–131.

Roos, J. E., Hellinger, J. C., Hallet, R., Fleischmann, D., Zarins, C. K. & Rubin, G. D. (2005). Detection of endograft fractures with multidetector row computed tomography, *J. Vasc. Surg.* 42(5): 1002–1006.

Rueckert, D., Sonoda, L., Hayes, C., Hill, D., Leach, M. & Hawkes, D. (1999). Nonrigid registration using free-form deformations: application to breast MR images, *Medical Imaging, IEEE Transactions on* 18(8): 712–721.

Stavropoulos, S. W. & Charagundla, S. R. (2007). Imaging techniques for detection and management of endoleaks after endovascular aortic aneurysm repair, *Radiology* 243(3): 641—655.

Teutelink, A., Muhs, B., Vincken, K. L., Wartels, L. W., Cornelissen, S. A., van Herwaarden, J. A., Prokop, M., Moll, F. L. & Verhagen, H. J. M. (2007). Use of dynamic computed tomography to evaluate pre- and postoperative aortic changes in AAA patients undergoing eneurysm repair, *J. Endovasc. Ther.* 14(1): 44–49.

Thirion, J. P. (1998). Image matching as a diffusion process: an analogy with maxwell's demons, *Medical Image Analysis* 2(3): 243–60.

Thodberg, H. H. (2003). Minimum description length shape and appearance models, *IN IMAGE PROCESSING MEDICAL IMAGING, IPMI* pp. 51—62.

van der Laan, M. J., Teutelink, A., Meijer, R., Wixon, C. L. & Blankensteijn, J. D. (2003). Noninvasive evaluation of the effectiveness of endovascular AAA exclusion, *Journal of Endovascular Therapy: An Official Journal of the International Society of Endovascular Specialists* 10(3): 458–462. PMID: 12932156.

van Herwaarden, J. A., Bartels, L. W., Muhs, B. E., Vincken, K. L., Lindeboom, M. Y., Teutelink, A., Moll, F. L. & Verhagen, H. J. (2006). Dynamic magnetic resonance angiography of the aneurysm neck: Conformational changes during the cardiac cycle with possible consequences for endograft sizing and future design, *J. Vasc. Surg.* 44(1): 22—28.

van Herwaarden, J. A., Muhs, B. E., Vincken, K. L., van Prehn, J., Teutelink, A., Bartels, L. W., Moll, F. L. & Verhagen, H. J. (2006). Aortic compliance following EVAR and the influence of different endografts: determination using dynamic MRA, *Journal of Endovascular Therapy* 13(3): 406—414.

Wells, W. M., III, Viola, P. & Kikinis, R. (1996). Multi-Modal volume registration by maximization of mutual information.

Williamson, E. E., Kirsch, J., Araoz, P. A., Edmister, W. B., Borgeson, D. D., Glockner, J. F. & Breen, J. F. (2008). ECG-Gated cardiac CT angiography using 64-MDCT for detection of patent foramen ovale, *American Journal of Roentgenology* 190: 929—933.

Wink, O., Niessen, W. & Viergever, M. (2004). Multiscale vessel tracking, *IEEE Trans Med Imaging* 23(1): 130–133.

Worz, S., Godinez, W. J., Rohr, K., Pluim, J. P. W. & Dawant, B. M. (2009). Segmentation of 3D tubular structures based on 3D intensity models and particle filter tracking, *Proc. of SPIE*, Vol. 7259, Lake Buena Vista, FL, USA, p. 72591P.

Xu, C. & Prince, J. L. (1998). Snakes, shapes and gradient vector flow, *IEEE Transactions on Image Processing* 7(3): 359—369.

Zarins, C. K., White, R. A., Schwarten, D., Kinney, E., Diethrich, E. B., Hodgson, K. J. & Fogarty, T. J. (1999). AneuRx stent graft versus open surgical repair of abdominal aortic aneurysms: multicenter prospective clinical trial, *J. Vasc. Surg.* 29(2): 292–305.

Zhou, C., Chan, H., Chughtai, A., Patel, S., Agarwal, P., Hadjiiski, L. M., Sahiner, B., Wei, J., Ge, J., Kazerooni, E. A., Giger, M. L. & Karssemeijer, N. (2008). Automated segmentation and tracking of coronary arteries in ECG-gated cardiac CT scans, *Proc. of SPIE*, Vol. 6915, San Diego, CA, USA, p. 69150O.

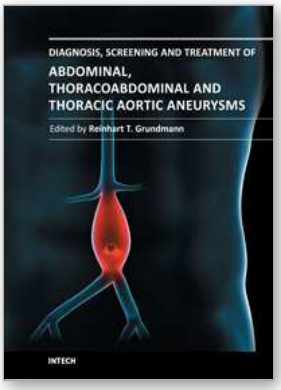

Diagnosis, Screening and Treatment of Abdominal, Thoracoabdominal and Thoracic Aortic Aneurysms
Edited by Prof. Reinhart Grundmann

ISBN 978-953-307-466-5
Hard cover, 414 pages
Publisher InTech
Published online 12, September, 2011
Published in print edition September, 2011

This book considers mainly diagnosis, screening, surveillance and treatment of abdominal, thoracoabdominal and thoracic aortic aneurysms. It addresses vascular and cardiothoracic surgeons and interventional radiologists, but also anyone engaged in vascular medicine. The high mortality of ruptured aneurysms certainly favors the recommendation of prophylactic repair of asymptomatic aortic aneurysms (AA) and therewith a generous screening. However, the comorbidities of these patients and their age have to be kept in mind if the efficacy and cost effectiveness of screening and prophylactic surgery should not be overestimated. The treatment recommendations which will be outlined here, have to regard on the one hand the natural course of the disease, the risk of rupture, and the life expectancy of the patient, and on the other hand the morbidity and mortality of the prophylactic surgical intervention. The book describes perioperative mortality after endovascular and open repair of AA, long-term outcome after repair, and the cost-effectiveness of treatment.

INTECH
open science | open minds

InTech Europe
University Campus STeP Ri
Slavka Krautzeka 83/A
51000 Rijeka, Croatia
Phone: +385 (51) 770 447
Fax: +385 (51) 686 166
www.intechopen.com

InTech China
Unit 405, Office Block, Hotel Equatorial Shanghai
No.65, Yan An Road (West), Shanghai, 200040, China
中国上海市延安西路65号上海国际贵都大饭店办公楼405单元
Phone: +86-21-62489820
Fax: +86-21-62489821